Journal of Engineering for Gas Turbines and Power. Received June 27, 2019;
Accepted manuscript posted August 13, 2019. doi:10.1115/1.4044487

GTP-19-1351
Effect of noise and nonlinearities on thermoacoustics of can-annular combustors

G. Ghirardo[1]*, **J.P. Moeck**[2] **M.R. Bothien**[1]
[1] Ansaldo Energia Switzerland
Römerstrasse 36, Baden 5401, Switzerland
[2] Department of Energy and Process Engineering,
Norwegian University of Science and Technology, Trondheim 7491, Norway

Can-annular combustors consist of N distinct cans set up symmetrically around the axis of the gas turbine. Each can is connected to the turbine inlet by means of a transition duct. At the turbine inlet a small gap between the neighbouring transition ducts allows acoustic communication between the cans. Thermoacoustic pulsations in the cans are driven by the respective flames, but also the communication between neighbouring cans through the gap plays a significant role. In this study we focus on the effect of the background noise intensity and of the nonlinear flame saturation. We predict how usually clusters of thermoacoustic modes are unstable in the linear regime and compete with each other in the nonlinear regime, each cluster consisting of axial, azimuthal and push-pull modes. Since linear theory cannot predict the nonlinear solution, stochastic simulations are run to study the nonlinear solution in a probabilistic sense. One outcome of these simulations are the various pulsation patterns, which are in principle different from one can to the next. We recover how a stronger flame response in one can can give rise to the phenomenon of mode localization, but also how the nonlinearity of the flame saturation and the competition between modes have an effect on the nonlinear mode shape. We finally predict the coherence and phase between cans on the linearized system subject to noise, and compare the predictions with engine measurements, in terms of spectra of amplitude in each can and coherence and phase, observing a good match.

INTRODUCTION

Can-annular combustors are common in heavy-duty land based gas turbines [1, 2]. In this design the air flows from the compressor outlet to the combustor plenum, where the air stream splits into N cans. In each can the fuel is injected with one or more fuel injectors, downstream of which one or more combustion zones are formed [2]. After the last combustion zone, the hot gas flows into the turbine inlet. Since the can cross section is circular and the inlet of the turbine is an annular gap, a special transition duct is designed to suitably link the two, as sketched in Fig. 1.

Due to the flame response to acoustic waves, a positive feedback loop can form between the acoustics of the combustion chamber and the flames, leading to self-excited thermoacoustic oscillations [4]. On a qualitative level, acoustic and thermoacoustic modes in can-annular and in annular systems share some similarity. This is because both configurations nominally feature discrete rotational symmetry. In this ideal symmetric case, most of the acoustic and thermoacoustic modes are degenerate, i.e., they have an additional degree of freedom with respect to their specific space–time structure (standing vs. spinning, nodal line orientation). However, the modal structure significantly differs. While in an annular combustor the lower-frequency modes are usually sufficiently spaced apart so that their interaction is not essential (exceptions exist in special cases [5]), can-annular systems generically exhibit clusters of closely spaced eigenvalues [3]. This feature can be attributed to the special structure of a can-annular combustor with its weakly coupled, nominally identical subsystems (the cans). It is known from structural vibration theory that such systems exhibit sets of closely spaced eigenvalues [6]. This spectral structure makes these systems highly sensitive to parametric perturbations and may give rise to the formation of localized modes if the nominal symmetry is perturbed [7]. It was shown in the recent work of Ghirardo *et al*. [3] that this may indeed be observed for thermoacoustic modes in can-annular systems with perturbed symmetry.

Recent work of Farisco, Panek *et al*. [8–10] studies in particular the acoustic communication between adjacent cans at the turbine inlet. The work of Ghirardo *et al*. [3], presented one year ago at the ASME Turbo EXPO 2018 in Oslo, focused especially on the acoustic response of transition ducts. Thermoacoustic dynamics in real engines are subject to significant levels of background noise, which perturb the system in a stochastic way [11–13]. The effect of noise on the ther-

*contact author: giulio.ghirardo@ansaldoenergia.com

Journal of Engineering for Gas Turbines and Power. Received June 27, 2019;
Accepted manuscript posted August 13, 2019. doi:10.1115/1.4044487

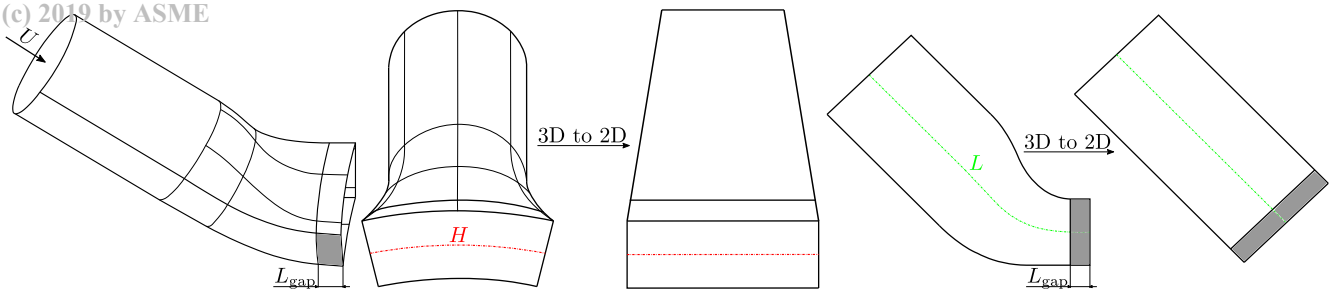

(a) 3D sketch of a transition duct (b) Front view of the air volume (c) Side view of the air volume

Fig. 1: Geometry of a typical transition duct and the simplifications leading to the 2D model discussed by [3]. The communicating gap between two adjacent transition ducts is colored in gray, with an axial length L_{gap}. At the turbine inlet, each transition duct covers a span H in the azimuthal direction. The nondimensional number governing the strength of the communication between the cans is L_{gap}/H. Figures from [3]

moacoustics of can-annular systems has not been considered yet.

In the present work, a qualitative model consisting also of a set of cans is discussed, with a focus on the dynamics of the whole system. We present a comparison between model and engine measurements, highlighting the effect of the background noise on the system dynamics. We tackle the problem by increasing the level of complexity from one section to the next. We consider first in the linear regime both the symmetric case and the non-symmetric case, discussing some new results on the sensitivity of the acoustics of can-annular systems. We then discuss the nonlinear case and the effect of noise, and compare this to engine data.

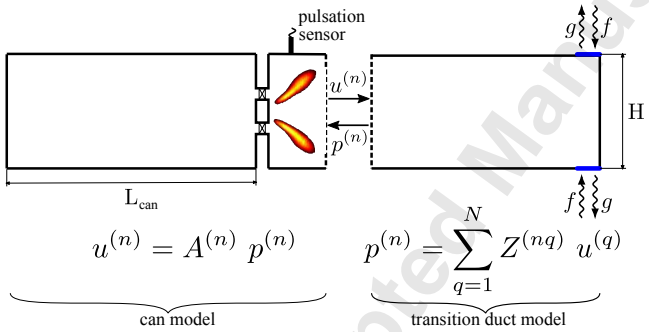

Fig. 2: Sketch of one can and respective transition duct. The full model consists of N blocks like this one, connected at the turbine inlet where the acoustic waves f and g travel through the two gaps drawn in blue on the right, with gap length L_{gap} as presented in Fig. 1. $Z^{(nq)}$ is the $N \times N$ impedance of the set of N transition ducts, with inputs the N acoustic velocities $u^{(q)}$ and output the N acoustic pressures $p^{(n)}$. On the upstream end of the transition ducts, these are related by the can admittance $A^{(n)}$

THE MODEL

The acoustic modelling of a set of N transition ducts communicating at the turbine inlet was discussed by [3], and only a brief description follows here. The model depends on three characteristic lengths reported in Fig. 1: the length L of the transition duct, the span H at the turbine inlet, and the length L_{gap} of the gap between adjacent cans, often referred to as cross-talk area. Full acoustic reflection at the turbine inlet is assumed because the flow is close to choked [14], and entropy waves' reflection and mean flow effects are neglected. We also focus on acoustic frequencies below the cut-on frequency of the duct, so that all modes considered are axial at the upstream end of the transition ducts and that a truncated series expansion of the Green function of the wave equation can be used efficiently to model the acoustic response of the set of transition ducts [15]. Because the mean azimuthal velocity U_θ just upstream of the turbine inlet is usually very small in can-annular combustors, we set it to zero. Under these assumptions the set of transition ducts is not just rotationally symmetric, but also reflection symmetric. This will affect the spectrum of the problem in the next section.

The full model accounts also for the N cans, each connected upstream of each transition duct as in Fig. 2. In particular, each can consists of a straight duct closed on the upstream end, a burner element that accounts for an area contraction and expansion, a flame and the transition duct. The area contraction and burner are modelled by means of an L-ζ model, which accounts for local acoustic damping occurring because of the pressure drop [16].

THE LINEAR SYMMETRIC CASE

Can-annular combustors are only to a first approximation rotationally symmetric, with each can not exactly the same as the other. This can occur for example because of small geometrical differences in the hardware leading to different mass flow rates between cans, azimuthal inhomogeneities in the air intake from the compressor into the combustor plenum, and inhomogeneities in the fuel distribution to each can. It is however useful to study the real-world, ro-

tationally non-symmetric case as a perturbation of the symmetric case, which is discussed in this section.

We consider $N = 12$ identical cans, with the n-th can at the azimuthal position

$$\theta_n = 2\pi n/N \qquad n = 1,2,\ldots,12 \tag{1}$$

When the system is symmetric, Bloch wave theory guarantees that the mode shapes in the frequency domain can be written as [17, 18]:

$$\hat{p}(\boldsymbol{x}) = \psi(\boldsymbol{x})e^{im\theta}, \qquad m = -N/2+1,\ldots,0,1,\ldots,N/2 \tag{2}$$

In (2), $\boldsymbol{x}$ denotes a point in the three-dimensional space, which in cylindrical coordinates corresponds to (r,θ,z), where the azimuthal coordinate θ goes from 0 to 2π. The function $\psi(\boldsymbol{x})$ is periodic in θ with a period $2\pi/N$, and describes the near-field solution. The solution p in all the cans is the near-field solution ψ modulated by the complex exponential $e^{im\theta}$, and except for $m = 0$ it is periodic in θ with period $2\pi/m$. For completeness, for $m = 0$ the solution p in (2) matches ψ and is periodic in θ with period $2\pi/N$. By direct substitution into (2) we observe that

- $m = 0$ corresponds to an axial mode, with the same amplitude and mode shape in each can.
- $m = N/2$ corresponds to a push-pull mode, with the same amplitude and mode shape in each can but opposite sign (each can is in anti-phase with its neighbours)
- other cases like $m = \pm n$ correspond to a rotating azimuthal wave of order n in the clockwise/anticlockwise direction

For this reason, we call m in (2) the azimuthal order of the solution, and we can classify all the solutions by their azimuthal order. We next consider the dependence of the eigenfrequencies of the system as function of the geometry, respectively the can length L_{can} and the gap length L_{gap}.

We calculate the frequencies and the growth rates of the system by means of a linear stability analysis for discrete values of L_{can}, while keeping L_{gap} constant. In Fig. 3 for each discrete value of L_{can} the frequencies are reported on the horizontal axis, with the azimuthal order of the respective mode shape appearing in the legend. In Fig. 3 and the following all angular frequencies have been normalized by dividing them by ω_0, which was chosen to have all frequencies of interest in the range between 0 and $3\omega_0/2$.

Because of the reflection symmetry of the system the eigenvalues of the azimuthal mode of order $+n$ and of the azimuthal mode of order $-n$ perfectly overlap and are degenerate. For simplicity, we report them simply as modes of order n in Fig. 3 and in the following. In Fig. 3 for a fixed value of L_{can} the markers appear in clusters that are close in frequency. In each cluster the mode at the lowest frequency is the axial mode, and the mode at the highest frequency is the push-pull mode. The visible clusters correspond to the first few axial modes of a single can system, which match the axial solution presented with a black triangle. For a fixed L_{can} the clusters are more compact as frequency increases, i.e. the 12 modes[1] in each cluster are closer together the larger is the frequency of the cluster. We observe that also in can-annular systems a longer length leads to a decrease of the frequency of the respective mode, as is typical of the axial modes in a one-dimensional duct as function of the duct length. In the following we fix L_{can} to a constant baseline value, for which the respective markers in Fig. 3 are empty.

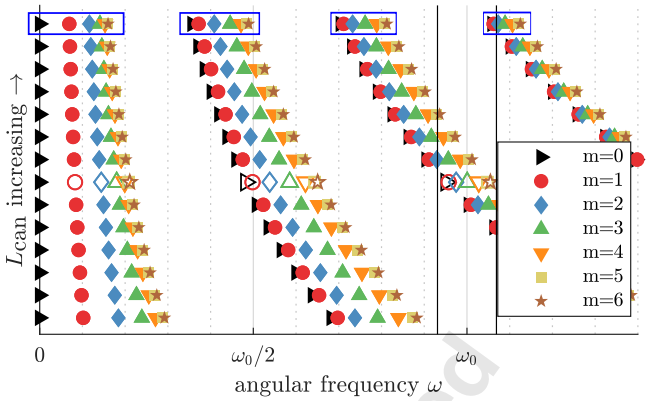

Fig. 3: Sensitivity of the purely acoustic frequencies of the system to the can length L_{can} described in Fig. 2. Each row of symbols corresponds to a stability analysis for a fixed value of L_{can} with the effect of the flame response switched off. We observe how modes appear in clusters, highlighted with blue boxes for the largest considered value of L_{can}. In each cluster there are modes with azimuthal order m varying from $m = 0$ to $m = 6$, as discussed after (2). The baseline case considered in the rest of the paper is reported with empty markers. Fig. 4 zooms in on the baseline cluster between vertical black lines and considers a different sensitivity

To study the sensitivity on L_{gap}, we zoom in on one cluster of the baseline case, in the frequency range in Fig. 3 between the two vertical black lines. The same cluster with empty markers appears in Fig. 4 for the baseline value of L_{gap}. We zoom in on one cluster because the gap length L_{gap} acts on each cluster of eigenmodes: in Fig. 4 the smaller the gap the closer are the frequencies of the cluster. In particular we observe that the frequency of the axial mode does not depend on L_{gap}, while the higher the azimuthal order of the mode m, the more its frequency departs from the axial frequency. We also observe that in the limit of $L_{\text{gap}} \to 0$ the frequencies of all the other modes of the cluster seem to tend to the frequency of the axial mode. Physically, this happens because in the limit of $L_{\text{gap}} \to 0$ the cans are not anymore communicating, and this would appear as $N = 12$ eigenmodes at the same exact eigenvalue, each with a localized mode shape in each can.

We present in Fig. 5 the predicted linear stability of the

[1] to these $N = 12$ modes correspond only $(N+1)/2 = 7$ markers in the figure. This is because 5 modes are degenerate and are presented with the same marker, and 2 modes ($m = 0, 6$) are not degenerate, for a total of 7 visible markers

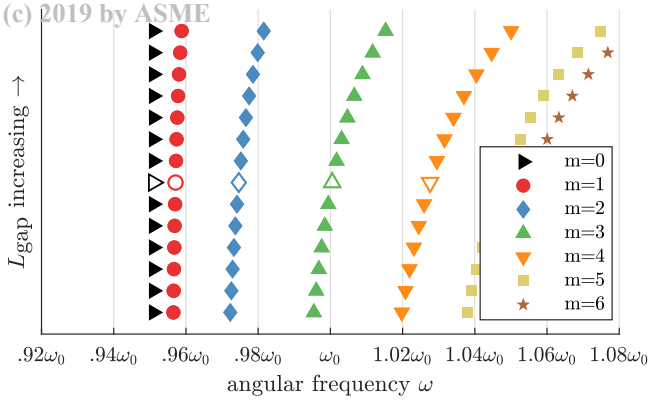

Fig. 4: Sensitivity of one of the clusters of Fig. 3 to the gap length L_{gap} between cans described in Fig. 1. Each row of symbols corresponds to a different value of L_{gap} and is obtained with the effect of the flame response switched off. The frequency of the axial $m = 0$ mode is unaffected by L_{gap}, and smaller values of L_{gap} lead to a narrower cluster. In the limit $L_{gap} \to 0$ all the eigenvalues of the cluster collapse on the axial mode, and each can oscillates by itself without interaction with the others. The baseline case considered in the rest of the paper is reported with empty markers, and coincides with the empty markers' cluster between vertical black lines in Fig. 3

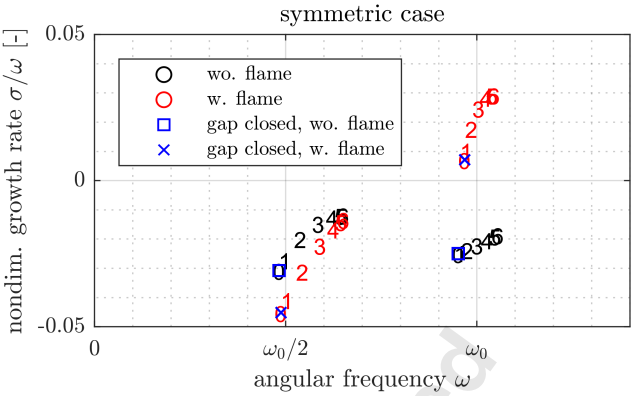

Fig. 5: Linear stability analysis for the symmetric case. Each marker/number is the eigenvalue of one thermoacoustic mode. The horizontal axis is the real part of the eigenvalue, the frequency in Hz of the mode. The vertical axis is the real part σ of the eigenvalue divided by the imaginary part ω, i.e. the nondimensional growth rate σ/ω. Positive values of σ correspond to linearly unstable thermoacoustic modes whose amplitude grows with time in the linear regime, while negative values correspond to stable modes whose amplitude diminishes in time, which are predicted to not be measured in a time domain simulation and in a test. The black markers correspond to the case when the effect of the flame response is switched off in the model and are all stable. When the flame response is switched on (red markers) some of these modes jump in the upper half plane and become unstable. The shapes of the most unstable modes for the case with the flame on are presented in Fig. 6. We present also with blue markers the prediction for the system when the gap is completely closed, with and without flame

system in terms of frequencies and growth rates, first with the flame response switched off in all cans (black numbers) and then switched on (red numbers). Instead of presenting each eigenvalue with a marker, we plot at the same position the integer of the respective azimuthal order m of the mode. The frequencies ω of the case without flame match the frequencies presented for the baseline case in Figs. 3 and 4, except for the cluster at the lowest frequency that is too damped to appear in Fig. 5. In the same figure we also present in blue the result obtained if we close all the gaps at the turbine inlet. In this symmetric case all cans are the same and their eigenvalues overlap exactly on the same blue markers and on the axial modes.

The respective mode shapes of the case with flame are presented in Fig. 6. We do not present the full spatial structure, but just the amplitude (height of the bars) and phase (color of the bars) of the acoustic pressure at the flame location in each can. For the modes with low azimuthal order $m = 1,2$ it is possible to distinguish by eye their azimuthal nature by just following the envelope of the amplitude of the mode along the annulus. We observe however that for $m \geq 3$, for a number of cans equal to $N = 12$ it is difficult to tell by eye the azimuthal order of the mode, because the wavelength is not much larger than the can spacing. For this specific case the most unstable mode is a push-pull mode at a frequency slightly larger than ω_0, but we also find that the whole cluster of eigenmodes close to ω_0 is unstable. It is then not possible, based only on the results of the linear stability analysis, to draw conclusions on the state of the system in the nonlinear regime.

THE LINEAR NON-SYMMETRIC CASE

In this section we perturb the rotational symmetry of the system, and consider an asymmetry in the flame response. An actual asymmetry, for example, the burner geometry, pressure loss or fuel injection, will generally affect both gain and phase (or time delay) of the flame response. Here, we only consider can-to-can variations in the gain and find that they reproduce the experimental observations.

Discussing a general loss of rotational symmetry of the flame response has already been done in the past in thermoacoustics. One analytic approach to the problem consists to use as ansatz the mode shape of the symmetric problem. The governing equations of the non-symmetric problem are then projected on this ansatz, and linear sensitivities of the eigenvalue are calculated [19]. This procedure assumes that the change of the shape of the mode of interest due to the loss of symmetry is negligible. This usually holds for azimuthal instabilities in annular combustors because there are no other modes that are close to the degenerate mode of interest[2] and

[2]indeed, annular combustors have azimuthal modes whose frequencies in a first approximation scale like $f_n = nc/\pi D$ $n = 1,2\ldots$, where c is the speed of sound and D is the diameter of the combustion chamber. It is clear from this expression that these modes are far from each other with a frequency spacing of $c/\pi D$ and do not form a cluster as modes in can-

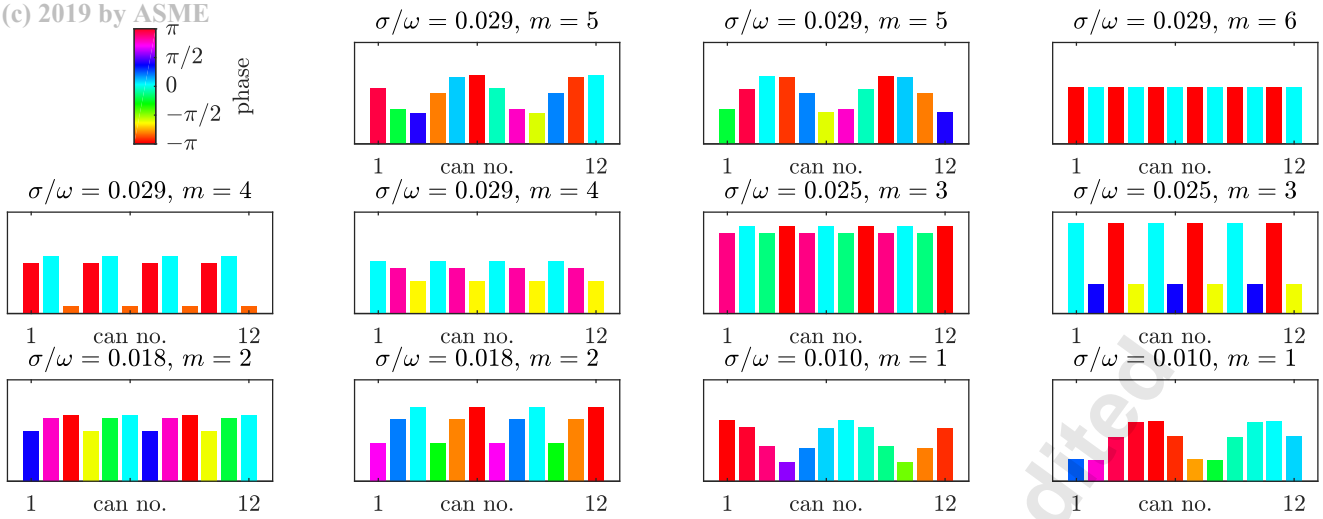

Fig. 6: Mode shapes of the symmetric case, with the flame response switched on, for the first 11 most unstable eigenmodes of the linear stability analysis with the flame on (red markers in Fig. 5). Each frame corresponds to an eigenmode, and the frames are ordered from left to right and top to bottom by decreasing value of the nondimensional growth rate σ/ω. In each frame each bar corresponds to one can. The height of the bar is the amplitude of the acoustic pressure of the thermoacoustic mode at the flame location, and the cans are ordered from 1 to $N = 12$ from left to right. The color of the bar is the phase difference between the pressure in the respective can and the can with the largest amplitude. In this case the system is symmetric: *1)* each eigenmode belongs to one azimuthal order m, appearing in the title of each frame; *2)* all modes with an order that is not multiple of $N/2 = 6$ come in degenerate pairs, and these two mode shapes may be arbitrarily combined in a linear fashion

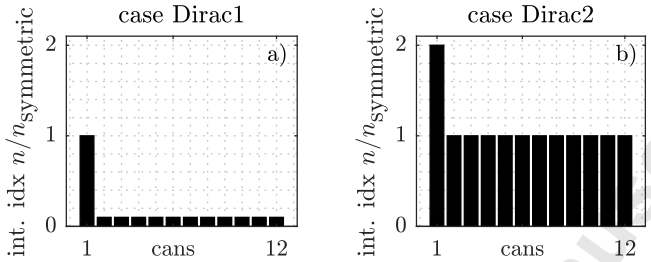

Fig. 7: Two perturbations considered in this paper. In the Dirac1 case, we decrease from the symmetric case the interaction index (the gain) of the flame response in all cans except can 1. In the Dirac2 case, we increase from the symmetric case the interaction index (the gain) of the flame response only in can 1

the sensitivity of the mode shape on a perturbation is small.

In can-annular combustors instead modes appear in clusters occupying a small frequency range. This leads to a strong sensitivity of the mode shapes to a perturbation, as discussed by Ghirardo *et al.* [3] and shown next. In that paper it is discussed how an increase of the flame response in just one can leads in the linearized system to a strong change of the mode shapes. In particular Ghirardo *et al.* found that in the linearized system one of the eigenmodes has a larger amplitude in the can with increased flame response. In the broader physics literature this phenomenon is called mode localization, and is common for systems undergoing a perturbation from a symmetric state [7, 23]. This linear result is consistent with experimental evidence of mode localization, as reviewed in the same paper [3]. In the present paper we discuss if this linear result applies also in the nonlinear regime, and under which conditions. We leave investigations of different losses of symmetry, like a can-to-can variation of the time delays governing the response of the flames, to future works.

We consider two similar cases in this paper, where only one can differs from the others. In a first case we decrease the flame response in all cans except can 1, by dividing the gains of their flame responses by 10, as presented in Fig. 7.a. We call this symmetry-breaking configuration Dirac1. We present in Fig. 8.a the linear stability predictions for this case. Only one can is linearly unstable if the gaps at the turbine inlet are closed (blue cross in the positive half plane around ω_0) while all other cans are stable (11 overlapping blue crosses in the negative half plane around ω_0). The whole system also presents just one eigenmode that is linearly unstable, the red number four. Notice that in this non-symmetric case the solutions do not have anymore the structure shown in (2), and the azimuthal orders presented in the figure are correct only in an approximate sense[3]. The shape of the most unstable eigenmode is presented in Fig. 9.a. We observe that the shape is strongly non-homogeneous, with a larger amplitude (bar height) in can 1, where the flame response is larger. As already discussed in [3], this is an example of mode local-

annular combustors. Notable exceptions include higher order degeneracies, as in [5, 20–22]

[3] the solution is projected on the azimuthal modes of every order, leading to $N/2+1 = 7$ projections. The azimuthal order of the projection with the maximum norm is represented in the Fig.

Journal of Engineering for Gas Turbines and Power. Received June 27, 2019;
Accepted manuscript posted August 13, 2019. doi:10.1115/1.4044487

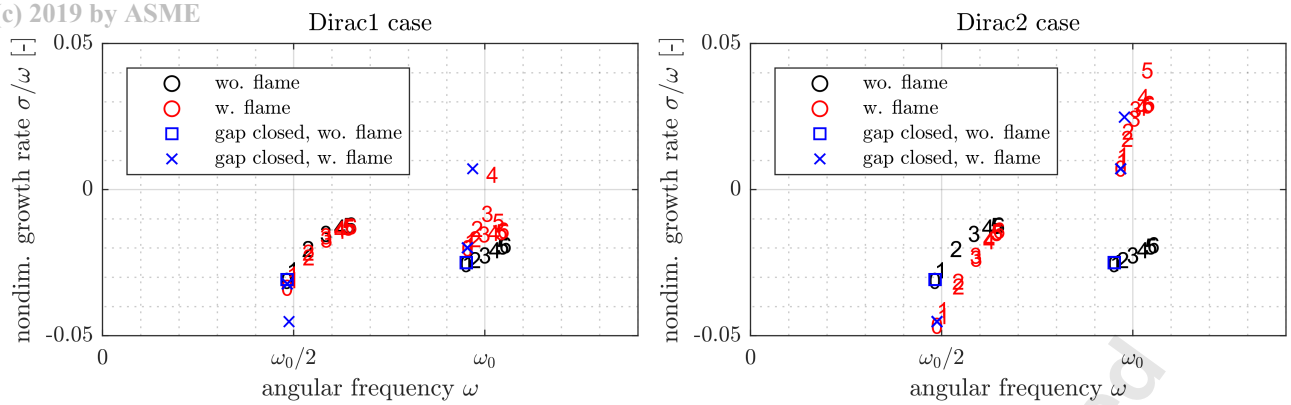

Fig. 8: Linear stability analysis for the non-symmetric cases Dirac1 (a) and Dirac2 (b). Same interpretation of Fig. 5 holds. In a) and b) the result for all the cans not communicating (blue markers) differ for different cans. In particular can 1 has a stronger flame response than the others and has a higher growth rate (highest blue cross around ω_0). in a) only one mode is linearly unstable, presented in Fig. 9.a. In b) many modes are linearly unstable at the same time, presented in Fig. 10

ization, where the mode is present with larger amplitude in a smaller region of the domain, in this case in can 1 and its closest neighbours.

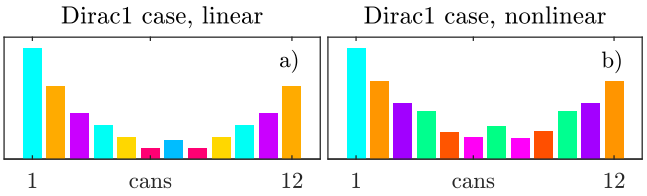

Fig. 9: example of mode localization in the linear and nonlinear regime for the case Dirac1 with the flame switched on. a) shape of the only unstable linear eigenmode of Fig. 8.a. b) dominant nonlinear mode shape, obtained from the time series of the stochastic simulation presented in Fig. 12.a at the peak frequency. In both a) and b) we observe that the mode shape has a larger amplitude in can 1, where the flame response is largest. The larger amplitude decreases moving away from can 1. The two mode shapes in a) and b) resembles well each other. Same colorbar and interpretation of Fig. 6 applies to both frames a) and b).

In a second case we increase the flame response only in can 1, by multiplying the gain of its flame responses by 2, as presented in Fig. 7.b. We call this symmetry-breaking configuration Dirac2. We present in Fig. 8.b the linear stability predictions. We observe how the loss of symmetry led to the splitting of each pair of degenerate azimuthal modes of the symmetric case of Fig. 5 into two distinct modes. One mode of the pair stays unchanged and matches the respective eigenvalue in Fig. 5 of the symmetric case. The other mode of the pair is instead affected by the symmetry loss. The same happens in an annular combustor with one damper only [24] or one burner only [25, §5]. The mode that is unchanged orients itself with an acoustic pressure node $p = 0$ in the perturbed can 1 at the flame location. In this way the product qp of fluctuating heat release rate q and acoustic pressure p contributing over 1 limit cycle to the Rayleigh criterion has trivially a zero contribution regardless of, and if, the flame in can 1 is perturbed. The other mode conversely orients itself with a pressure antinode in can 1 and the perturbation has the strongest effect on it. We present in Fig. 10 the mode shapes of the 11 most unstable modes.

We observe that the shape of the most unstable mode of the two cases Dirac1 and Dirac2, presented respectively in Fig. 9.a and in the top left frame of Fig. 10, are qualitatively very similar. The two non-symmetric cases however strongly differ in the number of modes being linearly unstable. In particular the case Dirac1 has only one mode in the positive half plane of Fig. 8.a, while the case Dirac2 has a whole cluster of modes in the positive half plane of Fig. 8.b. This has strong implications in the nonlinear regime, as we discuss in the next section.

THE NONLINEAR CASE AND THE EFFECT OF NOISE

In this section we run time domain simulations of the model and compare them with engine results and linear results. For running the simulations we need to describe the response of the flame in the nonlinear regime. We choose a simple saturation mechanism, and set the nonlinear heat release rate as

$$q_{\mathrm{nl}} = \kappa \arctan(q_{\mathrm{l}}/\kappa) \tag{3}$$

where q_{l} is the linear response of the flame discussed in the previous sections, and κ is a saturation constant, which does not affect the linear response of the heat release rate. This guarantees that the describing function of the heat release rate tends to zero at infinity.

To simulate the noisy fluctuations typical of the engine, we add a stochastic term in each can. This appears as an additional stochastic flame response that is independent of

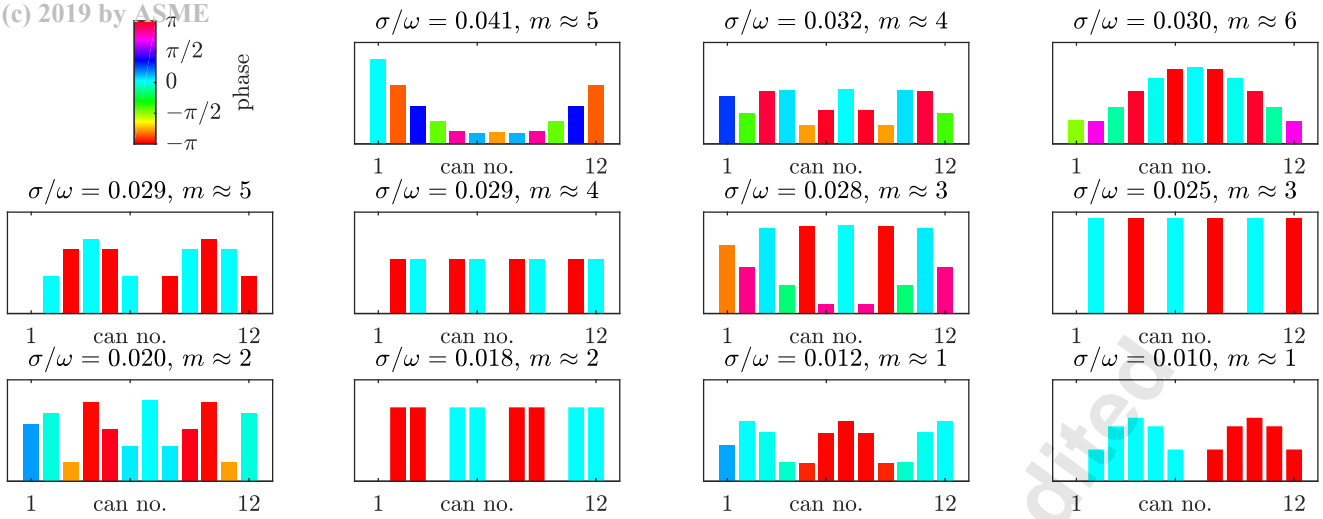

Fig. 10: Linear mode shapes for the Dirac2 case, with the flame response switched on. Same as Fig. 6 but for the first 11 most unstable eigenmodes of the linear stability analysis of the Dirac2 case of Fig. 8.b. In this case the system is not symmetric, and each mode belongs to a certain azimuthal order only in an approximate sense. We observe that the mode with the largest positive growth rate $\sigma/\omega = 0.041$ (top left frame) has a larger amplitude in can 1, where the flame response is largest. The larger amplitude decreases moving away from can 1. This is an example of mode localization, and is similar to the most unstable linear mode of the case Dirac1, presented in Fig. 9.a

the system dynamics. For simplicity, we force the system with white noise, band-pass filtered around the frequency ω_0. We do so because the model is tuned to be representative of the engine in the range of frequencies close to ω_0.

We present in Fig. 11.a the amplitude spectra of the acoustic pressures $\hat{p}^{(n)}(\omega)$ measured at the flame location as in Fig. 2 in the 12 modelled cans. For each sensor, the average amplitude spectra (continuous line) and the maximum spectra (dashed line) at each frequency are presented. One can spot how there is more than one peak in the spectrum of each sensor, approximately at the same frequencies of the red markers in Fig. 5.

We also consider the alternative representation of the acoustic field in terms of the azimuthal modes:

$$p_m = \frac{1}{N}\sum_{n=1}^{N} p^{(n)} e^{im\theta_n} \tag{4}$$

where θ_n was defined in (1). Eq. (4) matches, apart for a multiplicative term, the discrete Fourier transform of the discrete sequence $[p^{(1)}, p^{(2)}, \ldots, p^{(N)}]$. Alternatively, the p_m can be interpreted as the complex-valued coefficients of the Fourier series expansion of the discrete-valued function $p(\theta_n)$. Eq. (4) holds in time and frequency domain, and allows to map the state of the system from the space of the acoustic pressures $p^{(n)}$ in the cans $\{n = 1, 2, \ldots, 12\}$ to the space of the azimuthal modes p_m with the azim. order $\{m = 0, \pm 1, \ldots, \pm 5, 6\}$. It is always true that the description of the state of the system in terms of $\{p^{(n)}\}$ and in terms of $\{p_m\}$ is equivalent, by means of (4) and its inverse. Only in the symmetric case it is possible also to state that each eigenmode has always only one coefficient $\hat{p}_{m^\sharp}(\omega)$ that is non-zero, where $m^\sharp$ is its azimuthal order. In that case, the quantity $|\hat{p}_{m^\sharp}(\omega)|$ is the amplitude of the eigenmode. In the non-symmetric case however, one can in principle interpret $\{p_m\}$ only as a set of coefficients of a Fourier series expansion, without a guarantee that the eigenmodes have necessarily a mode shape that resemble a certain Fourier mode. Despite this technicality, we will call the p_m the azimuthal modes of the system.

We present in Fig. 11.b the amplitude spectra of the azimuthal modes calculated with (4) for the same simulation of Fig. 11.a. We observe how the maximum spectra of the azimuthal modes of the cluster follow the same trend of the growth rates of the respective cluster in Fig. 5. However the azimuthal mode of order $m = 4$ is the dominant mode because the respective average spectra is much larger than the others.

We then discuss the two non-symmetric cases, and rescale the intensity of the stochastic source in the same manner of the interaction index, as described in Fig. 7. In the case Dirac1 this means that we divided by 10 these source terms in all cans except in can 1. We present in Fig. 12 the calculated spectra for the Dirac1 case, and observe larger pulsations in can number 1 and its neighbours. We also identify[4] the nonlinear mode shape at the dominant frequency and present it in Fig. 9.b. There is good agreement between this nonlinear, identified mode shape with the most unstable linear mode in Fig. 9.a. This can be interpreted as follows. In the linear regime only one mode is linearly unstable, which in the nonlinear regime saturates to a limit cycle amplitude. The differences between the linear and nonlinear mode shapes are due to nonlinear effects.

We present in Fig. 13 the calculated spectra for the

[4] how this identification is carried out is discussed in detail in the next section

Journal of Engineering for Gas Turbines and Power. Received June 27, 2019;
Accepted manuscript posted August 13, 2019. doi:10.1115/1.4044487

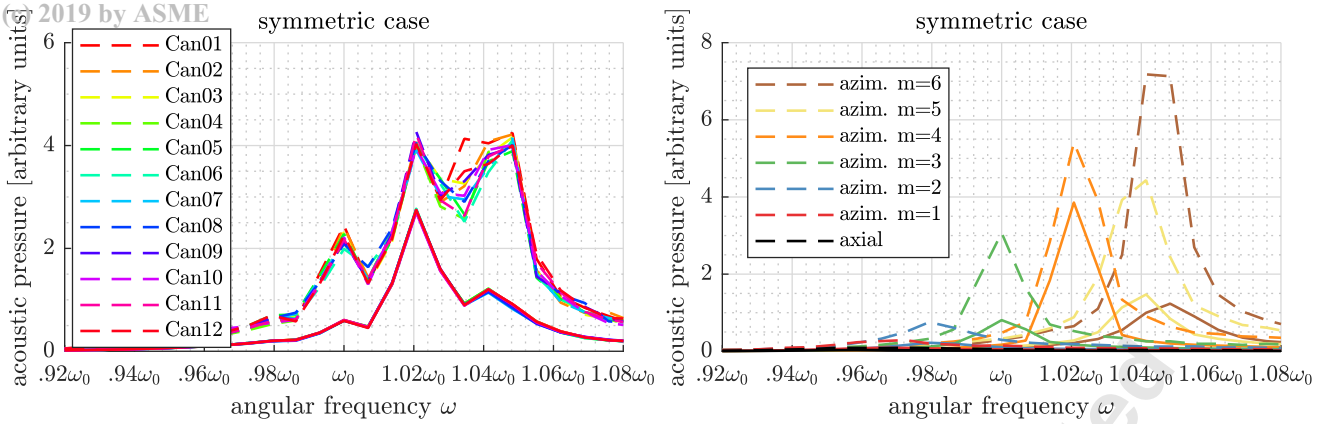

Fig. 11: Spectra for the simulated symmetric case. Amplitude spectra of the acoustic pressure from the timeseries of the simulation for the symmetric case. a) can space. b) azim. modes space. Dashed lines are the maximum spectra, while continuous lines are the average spectra

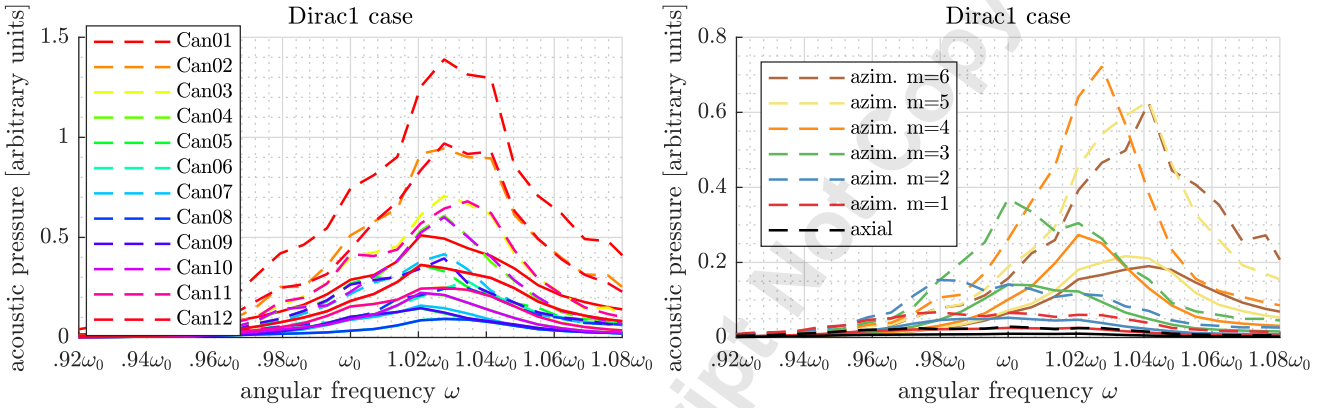

Fig. 12: Spectra for the simulated Dirac1 case. a) acoustic pressure in the cans. b) acoustic pressure in terms of the azim. modes. Dashed lines are the maximum spectra, while continuous lines are the average spectra

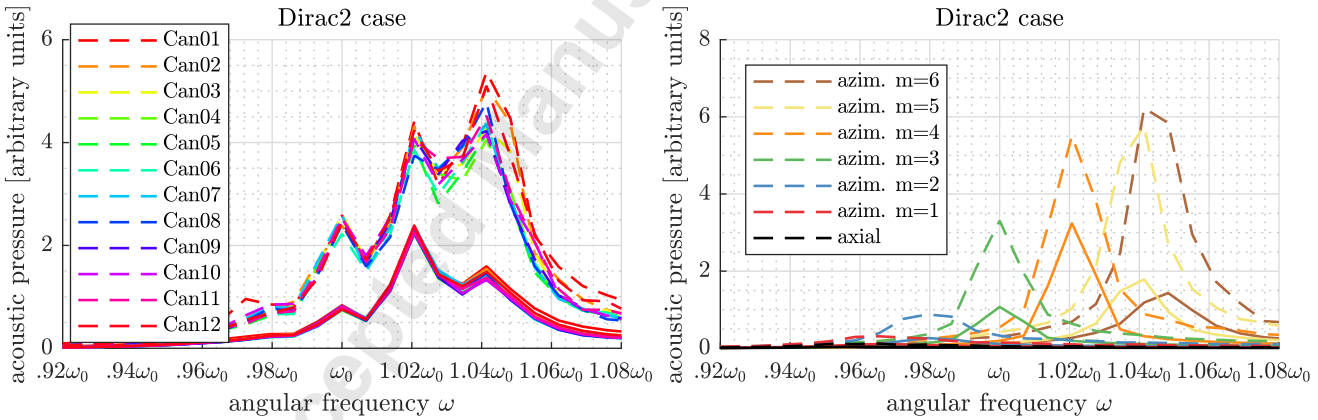

Fig. 13: Spectra for the simulated Dirac2 case. a) acoustic pressure in the cans. b) acoustic pressure in terms of the azim. modes. Dashed lines are the maximum spectra, while continuous lines are the average spectra

Dirac2 case, and identify in Fig. 14 the nonlinear mode shape at the two dominant frequencies of Fig. 13.a. The two nonlinear mode shapes do not resemble any of the linear mode shapes of Fig. 10. This can be interpreted as follows. In the linear and nonlinear regime many modes are unstable. The nonlinear mode shape is, in a weakly nonlinear sense, a linear combination of all unstable modes. Secondly, the shape of these modes is sensitive to perturbations, which arise naturally from the nonlinearities of the problem, and the mean mode shape is the result of all the modes competing with each other, subject to the background noise.

We also notice that the increased flame response in can

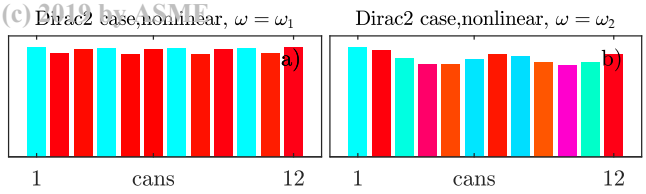

Fig. 14: We present in a) and b) the identified nonlinear mode shape estimated from the time-series of the Dirac2 case with the flame response switched on, at a fixed frequency. In particular a) and b) correspond each to the two highest peaks in Fig. 13.a at frequencies ω_1 and ω_2, with ω_1 the smallest frequency of the two. Neither of the two identified nonlinear mode shapes presented here resemble any of the linear mode shapes presented in Fig. 10

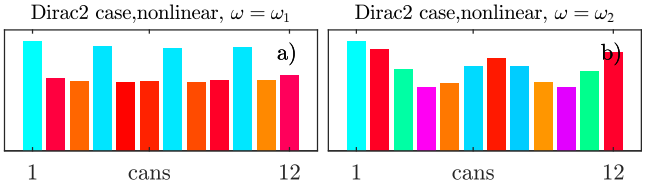

Fig. 15: Same as Fig. 14 but after rescaling the nonlinear saturation constant κ. The two frequencies ω_1 and ω_2 of the two highest peaks do not change with the rescaling of κ. The two patterns in a) and b) are similar to the two patterns of Fig. 14, but the higher amplitude in can 1 is now more pronounced, with a stronger departure of the pulsation pattern from the symmetric baseline, which is characterized by all bars at the same height

1 does not lead to a noticeable local increase of the pulsation amplitude, and to a modest increase of the overall pulsation level (compare Fig. 13.a and Fig. 11.a). In fact, despite the fact that the linear flame response in can 1 is twice as large, its nonlinearly saturated counterpart is less than twice as large as in the other cans at the limit-cycle amplitude because of the saturation (3). This means that the symmetry-breaking is weaker in the nonlinear regime than in the linear regime, because we kept the flame saturation the same in all cans. In this paragraph we then further investigate the effect of the nonlinearity on the solution. In general, the saturation of the flame response depends often on $u'/\overline{U}$, where u' is the acoustic velocity at a reference cross section close to the flame and $\overline{U}$ is the mean bulk velocity on the same cross-section. It is also often the case that stronger flame responses in the linear regime saturate to higher amplitudes $u'/\overline{U}$, see e.g. [26], but this is not a general rule. Under this assumption, we study what happens to the Dirac2 case if we make the flame in can 1 stronger also in the nonlinear regime, by multiplying κ in (3) by 2. For reasons of brevity, we do not present the spectra of this case, but just the identified mode shapes of the two dominant peaks in Fig. 15. The two peaks occur at the same two frequencies of the Dirac2 case of Fig. 13. We observe that this leads to a larger loss of rotational symmetry of the system as compared to the baseline Dirac2 case of Fig. 14, and also to a higher pulsation amplitude in can 1.

We then present in Fig. 16 the spectra from a can-annular engine with 12 cans. The sensors in this case are not at the same position of the model, but in the same relative position in each can, so that the symmetry of the system is preserved also in the observations. We observe a good agreement with the simplified model, both in terms of the shape of the spectra of the cans, frequency spacing between the azimuthal modes, trends as function of frequency and ratio between maximum spectra (dashed lines) and average spectra (continuous lines).

PREDICTION OF COHERENCE PATTERNS

For the derivation of the following theoretical results, the flames are assumed to act as stochastic monopole sources, to be uncorrelated among the different cans, and to have the same spectral power density. The following relations are also derived considering the system is linear. This is a fair assumption to make in those cases when the system is linearly stable and the level of background noise is sufficiently low to not push the system in the nonlinear regime, so that the linearized system is representative of the system dynamics.

Let p_j be the acoustic pressure measured in the j-th can. The coherence between the acoustic pressure measured in cans i and j is defined as:

$$C_{ij}(\omega) \equiv \frac{E[\hat{p}_i(\omega)\hat{p}_j(\omega)^*]}{\sqrt{E[|\hat{p}_i(\omega)|^2]E[|\hat{p}_i(\omega)|^2]}} \tag{5}$$

where the asterisk denotes complex conjugation, and $E[\hat{p}_i(\omega)\hat{p}_j(\omega)^*]$ is the cross-spectral density at frequency ω between the signal $p_i(t)$ and the signal $p_j(t)$. In the symmetric case, the spectral amplitudes $|\hat{p}_i|$ appearing in the denominator are the same in all cans. Assuming the system is ergodic and stationary, the expected values can be estimated by means of time averages:

$$C_{ij} = \frac{\overline{\hat{p}_i(\omega)\hat{p}_j(\omega)^*}}{\sqrt{\overline{|\hat{p}_i(\omega)|^2} \cdot \overline{|\hat{p}_j(\omega)|^2}}} \tag{6}$$

where the overbar denotes a time average over a sufficiently long observation window. The coherence can be calculated applying (6) to time simulations or engine measurements, and can be predicted using (5) from the model, as we discuss next.

From the model in Fig. 2, we can calculate the linear transfer function G between the N flame sources $\boldsymbol{s} \equiv [s_1, \ldots, s_N]$ placed at the flame positions $\boldsymbol{x}_\mathrm{f}$ and the acoustic pressures $\boldsymbol{p} \equiv [p_1, \ldots, p_N]$ at the flame position:

$$\hat{\boldsymbol{p}} = \boldsymbol{G}(\omega)\hat{\boldsymbol{s}} \tag{7}$$

In (7) the operator $\boldsymbol{G}(\omega)$ is the Green function $\boldsymbol{G}_\mathrm{f}(\boldsymbol{x}, \omega)$ evaluated at the flame position, i.e. $\boldsymbol{G}(\omega) \equiv \boldsymbol{G}_\mathrm{f}(\boldsymbol{x}_\mathrm{f}, \omega)$. If the sys-

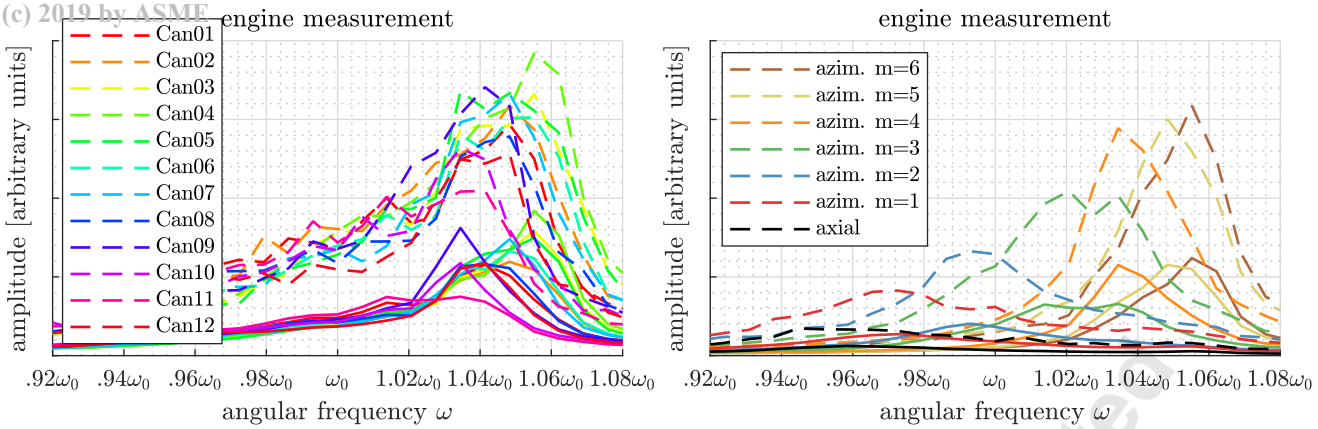

Fig. 16: Spectra for an engine measurement. Amplitude spectra of the acoustic pressure from engine data. a) can space. b) azim. modes space. Dashed lines are the maximum spectra, while continuous lines are the average spectra

tem exhibits discrete rotational symmetry, $\boldsymbol{G}$ is circulant. We can calculate next

$$\hat{\boldsymbol{p}}\hat{\boldsymbol{p}}^H = \boldsymbol{G}\hat{\boldsymbol{s}}(\boldsymbol{G}\hat{\boldsymbol{s}})^H = \boldsymbol{G}\hat{\boldsymbol{s}}\hat{\boldsymbol{s}}^H\boldsymbol{G}^H \tag{8}$$

where we neglect to write the explicit dependence on ω of all terms for convenience, and $\boldsymbol{p}^H$ denotes the Hermitian conjugate of $\boldsymbol{p}$. Because the noise sources are uncorrelated, we have that $E[\hat{\boldsymbol{s}}\hat{\boldsymbol{s}}^H] = \hat{s}^2\boldsymbol{I}$, where $\boldsymbol{I}$ is the identity matrix of size N, and $\hat{s}^2$ is the scalar noise power. The expected value of (8) simplifies to

$$E[\hat{\boldsymbol{p}}\hat{\boldsymbol{p}}^H] = \boldsymbol{G}\boldsymbol{G}^H\hat{s}^2 \tag{9}$$

The (i,j)-th element of (9) appears at the numerator of (5). Exploiting the symmetry, one can express the expected power $E[|\hat{p}_i(\omega)|^2]$ appearing at the denominator of (5) as

$$E[|\hat{p}_i(\omega)|^2] = E[\hat{p}_i(\omega)\hat{p}_i(\omega)^*] = \frac{1}{N}\sum_{i=1}^{N} E[\hat{p}_i(\omega)\hat{p}_i(\omega)^*] \tag{10}$$

$$= \frac{1}{N}E[\boldsymbol{p}^H\boldsymbol{p}] \tag{11}$$

Similarly we can calculate

$$\hat{\boldsymbol{p}}^H\hat{\boldsymbol{p}} = (\boldsymbol{G}\hat{\boldsymbol{s}})^H\boldsymbol{G}\hat{\boldsymbol{s}} = \hat{\boldsymbol{s}}^H\boldsymbol{G}^H\boldsymbol{G}\hat{\boldsymbol{s}} \tag{12}$$

By taking the expected value of (12) we obtain

$$E\left[\hat{\boldsymbol{p}}^H\hat{\boldsymbol{p}}\right] = s^2\,|\boldsymbol{G}|^2 \tag{13}$$

where $|\boldsymbol{G}|$ is the Frobenius norm of $\boldsymbol{G}$ (square root of the summed magnitude-squared elements). Finally, substituting (13) into (10) and (10) and (9) into (5) we obtain

$$\boldsymbol{C} = N\frac{\boldsymbol{G}\boldsymbol{G}^H}{|\boldsymbol{G}|^2} \tag{14}$$

We make use of (14) to predict the coherence pattern of the symmetric case with the flame response switched off. We present in Fig. 17 the pattern at the frequency of the modes of azimuthal order $m = 0,3,6$ in the black cluster close to ω_0 of Fig. 5, in terms of phase (angle of C_{ij}) and magnitude (absolute value of C_{ij}). In each of the three frames, each of the $12\times12 = 144$ squares represent a result between two sensors. Each square belonging to the top left triangular grid at position (i,j) represents the phase of C_{ij}, i.e. the phase difference between p_i and p_j. The same phase result for the square at position (j,i), which is the symmetric of (i,j), on the other side of the white diagonal, is not presented because it is trivially $C_{ji} = -C_{ij}$. Each square belonging to the bottom right triangular grid at position (i,j) presents instead the magnitude of the coherence. We focus for example on the first frame of Fig. 17, which was obtained at the frequency of the axial mode $m = 0$. Despite the frequency exactly matching the axial mode frequency, the phase pattern between cans is very different from the phase pattern typical of an axial mode (phase of zero between all pairs of cans). This happens because the other modes are very close in frequency to the axial mode, and then they also contribute significantly to this linear response. Similar observations can be made regarding the other two frames.

We can compare this with the engine result of Fig. 18, obtained using (6) on the timeseries presented in Fig. 16. In particular the coherence matrix (6) is evaluated at the frequency of the peaks of the modes of order $m = 0,3,6$ in Fig. 16.b. The comparison shows good qualitative agreement in terms of the coherence, despite violating the linear hypothesis of the prediction. The match in terms of phase difference is similar only for the push-pull mode ($m = 6$) in the third frame, while it is quite different for the other two frames. This does not come as a surprise. In fact, in Fig. 18 we observe the modal response of the system, which we describe next. In the first frame of Fig. 18 the phase pattern is mostly zero, as is typical for an axial mode. In the second frame we can observe three banded diagonal stripes of phase close to zero (light blue) and π (red), which is a pattern for a standing solution with fixed nodes in space. Finally, the third

frame shows a typical push-pull pattern, where the alternating light blue/red pattern shows the jump in phase of π from one can to the next. The three frames can also be ordered by increasing level of clarity of the pattern from the first (left) to the third frame (right). This corresponds to the increasing dominance of the respective modes of order $m = 0, 3, 6$ at their peak frequency in Fig. 16.b as compared to the other modes.

When considering the differences between Figs. 17 and 18, we stress that Fig. 17 captures the whole system (linear and stable) response to the excitation of the background noise, while Fig. 18 captures the modal response of the dominant mode of the system (nonlinear and unstable) subject to background noise.

CONCLUSIONS

We discuss a model for low-frequency thermoacoustics in can-annular combustors. Because of the approximate rotational symmetry of the system and the weak coupling occurring at the turbine inlet between adjacent cans, thermoacoustic modes appear in clusters. Each cluster contains modes of azimuthal order $m = 0, \pm 1, \pm 2, N/2$ for a can combustor with an even number N of cans. Each mode is axial in the main body of the can and azimuthal at the turbine inlet. The frequency spacing of the cluster, i.e. how tightly packed together are the modes of the cluster, is governed by the strength of the can-to-can coupling, which depends on an effective gap length L_{gap} at the turbine inlet, as presented in Fig. 1. As the gap becomes smaller, in each cluster the frequencies of the modes approach the frequency of the axial mode, which remains unchanged.

When one considers the effect of the flame on the system, we observe that usually all the modes of a cluster become unstable together at a given frequency, as exemplified in Fig. 5. The linear stability analysis cannot then in principle predict which eigenmode will take over in the nonlinear regime. To overcome this problem, we run stochastic dynamical simulations of the system. The results of the simulations are studied in terms of average and maximum spectra, and compared with engine measurements. Shapes of the spectra, spacing of the peaks within a cluster, and the ratio between maximum and average spectra show good agreement with the tuned model.

A pattern where the flame response of one can is increased is investigated. If this stronger flame in one can leads to only one unstable mode (case Dirac1), we observe mode localization in the nonlinear numerical simulations, as discussed in previous work based on linear analyses and experimental observations [3]. This mode localization consists in an increased pulsation amplitude in one can and its closest neighbours as compared to the other cans. If instead many modes are unstable at the same time (case Dirac2), this mode localization is present in the linear analysis of the system, but may or may not appear in the nonlinear regime as function of the saturated state of the system in the nonlinear regime. We have observed for two cases how the nonlinear mode shape is completely different from the shapes of the linear eigenmodes. This shows that dynamical simulations of the system are needed to be predictive on the nonlinear state of the system.

Finally, we considered the dynamics of a stable thermoacoustic mode excited by background noise. Assuming a linear system, the coherence and the phase between cans is predicted. This is compared with estimates of the same quantity on the nonlinear unstable modes of the engine measurements. Despite the fact that the system is unstable and nonlinear, we find good qualitative agreement in terms of the magnitude of the coherence between cans, and some agreement in terms of the phase between cans.

References

[1] Bethke, S., Krebs, W., Flohr, P., and Prade, B., 2002. "Thermoacoustic Properties of Can Annular Combustors". In 8th AIAA/CEAS Aeroacoustics Conference & Exhibit, paper no. AIAA 2002-2570, American Institute of Aeronautics and Astronautics, pp. 1–11.

[2] Pennell, D. A., Bothien, M. R., Ciani, A., Granet, V., Singla, G., Thorpe, S., Wickstroem, A., Oumejjoud, K., and Yaquinto, M., 2017. "An introduction to the Ansaldo GT36 constant pressure sequential combustor". In Proceedings of ASME Turbo Expo, paper no. GT2017-64790, pp. 1–11.

[3] Ghirardo, G., Di Giovine, C., Moeck, J. P., and Bothien, M. R., 2018. "Thermoacoustics of can-annular combustors". *Journal of Engineering for Gas Turbines and Power,* **141**(011007).

[4] Keller, J. J., 1995. "Thermoacoustic oscillations in combustion chambers of gas turbines". *AIAA Journal,* **33**(12), pp. 2280–2287.

[5] Bourgouin, J.-F., Durox, D., Moeck, J. P., Schuller, T., and Candel, S., 2014. "A new pattern of instability observed in an annular combustor: The slanted mode". *Proceedings of the Combustion Institute,* **35**(3), pp. 3237–3244.

[6] Pierre, C., and Cha, P. D., 1989. "Strong Mode Localization in Nearly Periodic Disordered Structures". *AIAA Journal,* **27**(2), pp. 227–241.

[7] Pierre, C., 1988. "Mode localization and eigenvalue loci veering phenomena in disordered structures". *Journal of Sound and Vibration,* **126**(3), pp. 485–502.

[8] Farisco, F., Panek, L., Janus, B., and Kok, J. B. W., 2015. "Numerical Investigation of the Thermo-Acoustic Influence of the Turbine on the Combustor". In Proceedings of ASME Turbo Expo, paper no. GT2015-42071, ASME, pp. 1–10.

[9] Panek, L., Huth, M., and Farisco, F., 2017. "Thermoacoustic characterization of can-can interaction of a can-annular combustion system based on unsteady CFD LES simulation". In Proceedings of the 1st Global Power and Propulsion Forum, paper no. GPPF-2017-81, pp. 1–5.

[10] Farisco, F., Panek, L., and Kok, J. B., 2017. "Thermoacoustic cross-talk between cans in a can-annular com-

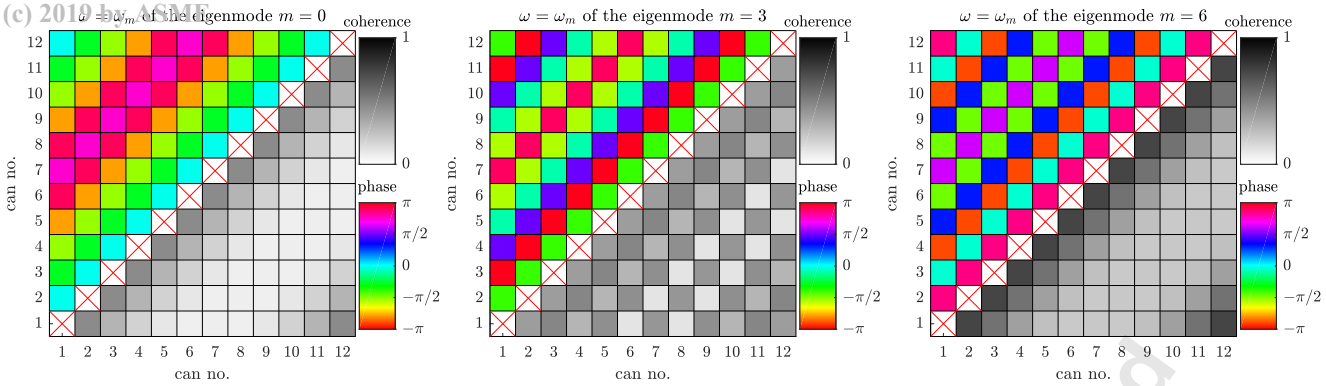

Fig. 17: Phase (top left triangular matrix) and absolute value (bottom right triangular matrix) of the coherence between acoustic pressure signals in the cans of the model, at the frequencies of the three modes of azimuthal order $0, 3, 6$. On the diagonal no value is shown. This Figure captures the response of the whole system, linearized and stable, to the excitation of uniform background noise

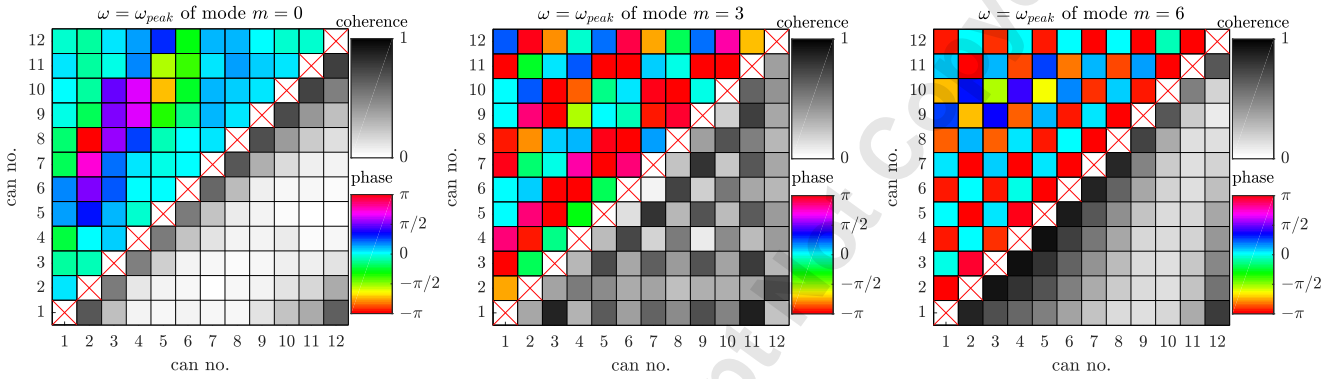

Fig. 18: Phase (top left triangular matrix) and absolute value (bottom right triangular matrix) of the coherence between acoustic pressure signals in the cans of the engine, for three modes of azimuthal order $0, 3, 6$, for the same self-excited state presented in Fig. 16. On the diagonal no value is shown. In each frame, the frequency at which the phase and the magnitude of the coherence is estimated is selected as the peak frequency of the azimuthal modes of order $m = 0, 3, 6$ in Fig. 16.b. In the third frame, the larger coherence between cans 3,4,5 corresponds to the higher amplitudes present in these cans at this frequency. This Figure captures the modal nonlinear response of the system, of the modes with azimuthal order $m = 0, 3, 6$.

bustor". *International Journal of Spray and Combustion Dynamics,* **9**(4), pp. 452–469.

[11] Lieuwen, T., 2003. "Statistical characteristics of pressure oscillations in a premixed combustor". *Journal of Sound and Vibration,* **260**(1), pp. 3–17.

[12] Noiray, N., and Schuermans, B., 2013. "On the dynamic nature of azimuthal thermoacoustic modes in annular gas turbine combustion chambers". *Proceedings of the Royal Society A: Mathematical, Physical and Engineering Sciences,* **469**(20120535), pp. 1–15.

[13] Ghirardo, G., Boudy, F., and Bothien, M. R., 2018. "Amplitude statistics prediction in thermoacoustics". *Journal of Fluid Mechanics,* **844**, pp. 216–246.

[14] Marble, F. E., and Candel, S., 1977. "Acoustic disturbance from gas non-uniformities convected through a nozzle". *Journal of Sound and Vibration,* **55**(2), pp. 225–243.

[15] Morse, P. M., and Feshback, H., 1953. *Methods of theoretical physics - Volume 2*. McGraw-Hill, New York, Toronto, London.

[16] Schuermans, B., Polifke, W., and Paschereit, C. O., 1999. "Modeling transfer matrices of premixed flames and comparison with experimental results". In Proceedings of ASME Turbo Expo 1999, paper no. 99-GT-132, ASME, pp. 1–10.

[17] Brillouin, L., 1953. *Wave propagation in periodic structures: electric filters and crystal lattices*, 2nd ed. Chapter VIII, pp. 139-140, Dover publications, Mineola, New York.

[18] Mensah, G. A., and Moeck, J. P., 2016. "Efficient computation of thermoacoustic modes in annular combustion chambers based on Bloch-wave theory". *Journal of Engineering for Gas Turbines and Power,* **138**, p. 081502 (7 pages).

[19] Noiray, N., Bothien, M. R., and Schuermans, B., 2011. "Investigation of azimuthal staging concepts in annular gas turbines". *Combustion Theory and Modelling,* **15**(5), pp. 585–606.

[20] Orchini, A., Mensah, G. A., and Moeck, J. P., 2018. "Effects of Nonlinear Modal Interactions on the Ther-

moacoustic Stability of Annular Combustors". *Journal of Engineering for Gas Turbines and Power,* **141**(2), p. 021002.

[21] Dong, Y., and Morgans, A. S., 2018. "Low-order network modeling for annular combustors exhibiting longitudinal and circumferential modes". In Proceedings of ASME Turbo Expo, paper no. GT2018-76506, ASME, pp. 1–12.

[22] Moeck, J. P., Durox, D., Schuller, T., and Candel, S., 2018. "Nonlinear thermoacoustic mode synchronization in annular combustors". *Proceedings of the Combustion Institute,* **000**, pp. 1–8.

[23] Triantafyllou, M. S., and Triantafyllou, G. S., 1991. "Frequency coalescence and mode localization phenomena: a geometric theory". *Journal of Sound and Vibration,* **150**(3), pp. 485–500.

[24] Stow, S. R., and Dowling, A. P., 2003. "Modelling of circumferential modal coupling due to Helmholtz resonators". In Proceedings of ASME Turbo Expo, paper no. GT2003-38168, ASME, pp. 1—-9.

[25] Parmentier, J.-F., Salas, P., Wolf, P., Staffelbach, G., Nicoud, F., and Poinsot, T., 2012. "A simple analytical model to study and control azimuthal instabilities in annular combustion chambers". *Combustion and Flame,* **159**(7), pp. 2374–2387.

[26] Ghirardo, G., Ćosić, B., Juniper, M. P., and Moeck, J. P., 2015. "State-space realization of a describing function". *Nonlinear Dynamics,* **82**(1-2), pp. 9–28.